

LArTPC hit-based topology classification with quantum machine learning and symmetry

Callum Duffy^{1†}, Marcin Jastrzebski^{1†}, Stefano Vergani^{1*}, Leigh H. Whitehead², Ryan Cross³, Andrew Blake⁴, Sarah Malik¹, John Marshall³

¹Department of Physics and Astronomy, University College London, London, UK.

²Cavendish Laboratory, University of Cambridge, Cambridge, UK.

³Department of Physics, University of Warwick, Coventry, UK.

⁴Physics Department, Lancaster University, Lancaster, UK.

*Corresponding author(s). E-mail(s): s.vergani@ucl.ac.uk;

†These authors contributed equally to this work.

Abstract

We present a new approach to separate track-like and shower-like topologies in liquid argon time projection chamber (LArTPC) experiments for neutrino physics using quantum machine learning. Effective reconstruction of neutrino events in LArTPCs requires accurate and granular information about the energy deposited in the detector. These energy deposits can be viewed as 2-D images. Simulated data from the MicroBooNE experiment and a simple custom dataset are used to perform pixel-level classification of the underlying particle topology. Images of the events have been studied by creating small patches around each pixel to characterise its topology based on its immediate neighbourhood. This classification is achieved using convolution-based learning models, including quantum-enhanced architectures known as quantum convolutional neural networks. The quantum convolutional networks are extended to symmetries beyond translation. Rotational symmetry has been incorporated into a subset of the models. Quantum-enhanced models perform better than their classical counterparts with a comparable number of parameters but are outperformed by classical models, which contain an order of magnitude more parameters. The inclusion of rotation symmetry appears to benefit only large models and remains to be explored further.

Keywords: quantum computing, quantum machine learning, deep learning, neutrinos, reconstruction, topology classification

1 Introduction

Liquid Argon Time Projection Chamber (LArTPC) detectors are commonly used in neutrino physics and represent the state of the art of this field. Although there are differences in the design, they normally comprise a cryostat filled with high-purity liquid argon kept at 87 K, a system to apply an internal electric field,

a readout mechanism made with wires, and a photon detection system. In LArTPCs, charged particles interact with argon nuclei, liberating electrons through ionisation. These electrons drift in an electric field towards readout wires, where they are detected. Combining the wire number with the time of detection, especially if the scintillation light is used as a trigger, gives spatial

and time information in a 2-D view. Calorimetric information is added to each 2-D view. The interactions of neutrinos with the argon nuclei are inferred by the presence of charged particles produced in the interaction emerging from a common vertex. The Micro Booster Neutrino Experiment (MicroBooNE) [1, 2] employed an 85 metric tons LArTPC detector to perform precision physics measurements and collected five years of data from 2016 to 2021. The experiment primary scientific goals were to solve the puzzle of the MiniBooNE low energy excess [3], to measure different neutrino cross sections, and to search for astrophysical phenomena. It was part of the wider Short Baseline Neutrino (SBN) [4], an ambitious program at Fermi National Accelerator Laboratory (FNAL) aimed at investigating eV-scale sterile neutrinos, neutrino-nucleus interactions at the GeV energy scale, and the advancement of the liquid argon detector technology. The Deep Underground Neutrino Experiment (DUNE) [5] represents the next generation of neutrino physics experiments, and is partly located at the Long-Baseline Neutrino Facility (LBNF) at FNAL and partly at Sanford Underground Research Facility (SURF). It aims to answer fundamental questions in particle physics, such as the neutrino mass ordering [6], the value of the charge-parity (CP)-violating phase [7], the formation of black holes after a supernova explosion [8], and the hypothetical proton decay [9]. The far detector (FD), one of the components of DUNE, will also utilise LArTPC technology [10], which has successfully been used in a number of recent experiments [11–15]. Of particular interest in long-baseline neutrino oscillation experiments is the ratio of electron to muon neutrinos arriving at the detector, making the primary task in such experiments reconstructing and identifying events as muon neutrino or electron neutrino events. To do so, the spatial details of the event captured need to be understood thoroughly. An accurate classification of each of the signals received is thus paramount. This work will make use of the MicroBooNE open dataset [16], but the longer-term objective of the project is to provide tools for processing data recorded by the DUNE-FD.

Pandora [17–19], typically run as part of LArSoft[20] workflows, is one of the most popular reconstruction frameworks for LArTPC experiments. It has a modular approach where each

algorithm performs a specific, and typically small, task. In this way, it is easier to guarantee that each step is done correctly. One of the most important steps is to separate track and shower-like topologies at the hit level, a crucial task to perform particle identification and event reconstruction. In order to do so, Pandora makes extensive use of machine learning (ML) techniques throughout the reconstruction chains. ML and deep learning (DL) have also been utilised in the MicroBooNE experiment, and there are several proposed applications of these techniques in DUNE [21–24]. Different approaches to separate track-like particles travelling through dense electromagnetic showers have been explored [25–27], but it remains one of the many open reconstruction problems where an increase in the performance is still sought after. The presented work contributes to this important subroutine.

The exploration of ever more capable machine learning models and recent rapid advancements in quantum technologies led to the birth of quantum machine learning (QML). One common critique of the current QML research is that models which appear successful are often benchmarked on simple problems [28, 29]. This study is interested in a real open problem in experimental neutrino physics, which remains unsolved by current machine learning methods. Previous QML uses in LArTPC experiments have been proposed in the context of event classification [30, 31] as well as event generation [32]. Together with many other early studies investigating the use of quantum computers in high energy physics (HEP), the community is an active contributor to the development of quantum technologies whilst being posed to be their great beneficiary [33].

A high-level introduction to the field of QML is given in Section 2. In Section 3, a detailed description of the LArTPC datasets used can be found. Section 4 discusses model design concepts, and the quantum and classical architectures used are described in Section 5. In Section 6, one can find the results of applying the best-found models to the problems.

2 Quantum Machine Learning

Quantum machine learning has emerged as one of the most promising families of quantum algorithms. It has garnered significant attention due to

the success and widespread adoption of classical machine learning and the compatibility of QML methods with noisy intermediate-scale quantum (NISQ) [34] devices. Combining these factors makes QML a particularly attractive avenue for exploring quantum computational advantages in practical settings.

While the search for practical quantum advantages in QML remains an active area of research, significant strides have been made theoretically [35–40]. These advances, combined with scrupulous dequantization studies [41], continue to refine our understanding of the field’s potential and its limitations. Empirically, small hints of potential advantage of quantum models appear in the form of better performance or similar performance with fewer parameters [31, 42–44]. It is crucial, however, to state that benchmarking quantum models against classical ones is, in general, a difficult task [29]. We find ourselves in a time where classical simulations of QML pipelines are prohibitively complex beyond 10s of qubits but quantum hardware is not yet ready to train big quantum models, either. What we can do in the meantime is understand the models we work with well and test them on challenging, real-life problems.

A critical consideration in the design of quantum learning models is their inductive bias, which refers to the assumptions embedded in the model architecture that influence its generalisation capabilities. This principle is the focus of geometric [45–47] and scientific [48–50] QML, where domain knowledge is incorporated into model design to enhance performance and interpretability.

The model used in this study is the well-known quanvolutional neural network which has been extended, for the first time, to include symmetries beyond translation. Quanvolutional neural networks allow one to study relatively large problems, compared to, for example, the quantum convolutional neural network (QCNN) [51], as quantum computation is required only for a small subroutine of the full forward pass. The models process data mostly classically and use only small circuits on local patches of a data point. Details of the model can be found in Section 4.2.

3 Datasets

Topologies seen in LArTPC images fall into two main categories: tracks and showers. Tracks are

linear structures, whereas showers are dense collections of non-zero pixels. Showers are produced by electromagnetic cascades induced by electrons (e^-), positrons (e^+) and photons (γ), whereas other particles such as muons (μ^\pm), charged pions (π^\pm) and protons (p) produce tracks. Clear examples of tracks and showers can be seen in Figure 1. This study uses two LArTPC datasets to test the efficacy of QML in hit-based topology classification.

The first is the openly available MicroBooNE dataset [2, 52], which is described in detail in Section 3.1. The second is an original dataset produced specifically for this study. It is made up of events where a muon and an electron are produced at the same vertex but at various opening angles. It allows us to easily control the “difficulty” of classification of the events produced. Intuitively, the smaller the angle between the two particles, the “denser” the events created are. Details of this dataset can be found in Section 3.2.

3.1 MicroBooNE open dataset

This dataset consists of approximately 750,000 events simulated in the MicroBooNE detector, featuring neutrino interactions producing electrons, photons, muons, charged pions, and protons and overlaid real cosmic rays. The MicroBooNE experiment is a LArTPC neutrino detector, which operated as part of Fermilab’s SBN programme. The detector is positioned on the surface, which results in a significant background of cosmic-ray-induced particles, predominantly muons. Due to its long integration time, MicroBooNE detector collects ionisation over an extended drift length, further amplifying cosmic-ray contamination. However, these cosmic-ray-induced particles have been removed for this study to ensure that the analysis focuses on distinguishing neutrino-induced track and shower events. Moreover, this is to align the study more closely with DUNE, where the cosmic ray background will not be present.

Each event in the dataset is represented as a set of three two-dimensional images, one for each wire readout plane: two induction planes (U and V), each consisting of 2400 wires, and a collection plane (Y) with 3456 wires. The induction planes are oriented at $\pm 60^\circ$ relative to the collection plane, whose wires run vertically. The wire spacing is 3 mm for all planes. In each image, the

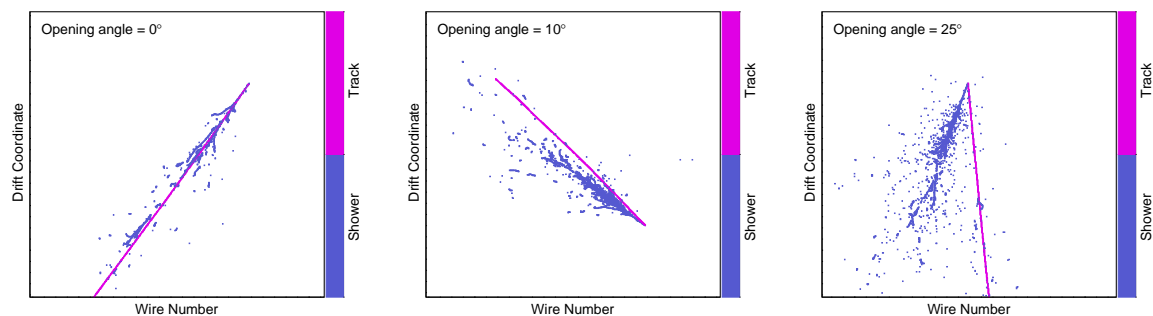


Fig. 1 Three example events containing one electron and one muon produced at a common vertex position. The events are seen projected into one of the three readout views, and the projected opening angle is given. Shower-like energy deposits in the electron-initiated electromagnetic shower and the small ionisation electrons along the muon track are shown in purple, and the energy deposits coming directly from the muon are shown in magenta.

x -axis corresponds to the wire number, while the y -axis represents the drift time. Pixel intensity is proportional to the number of ionized electrons reaching that position and time, effectively encoding energy deposition information. The effective pixel resolution is 3.3 mm in the drift (y) direction and 3 mm in the wire (x) direction, as the waveform is integrated over six TPC time-ticks ($3 \mu\text{s}$).

The goal of this work is to separate track and shower topologies. To facilitate training, we subdivide event images into $N \times N$ pixel patches (See Figure 2). Mimicking the approach used in another study [25], a patch around each hit is built, with the chosen hit in the centre of the patch. Features of that patch are analysed to determine whether the central pixel is track or shower-like. By repeating this process for each hit in the image, the algorithm is able to characterise each hit in the image as track or shower-like. Based on the simulation labels, each patch is assigned a label based on the particle that contributes most to the intensity of the central pixel. While multiple charged particles can deposit charge at the same location, we adopt a single-particle labelling scheme, which has been shown to be beneficial for downstream tasks [53]. At this initial stage of reconstruction, rather than identifying the specific particle responsible for the signal, each deposit is classified as track-like (label 0) or shower-like (label 1). This labelling scheme is well-motivated, as each charged particle produces either a track-like or shower-like signature.

3.2 Neutrino-like dataset

The aim of this dataset is to create events with one shower-like and one track-like particle emanating from a common vertex with a variable opening angle between them. This was performed using LArSIMple, a simple LArTPC detector simulation [54] based on Geant4 v4_11_1_p01ba [55]. An electron was created with its direction randomly chosen from an isotropic distribution, and a muon was created within a cone of a variable opening angle around the direction of the electron. Together, these two particles produce interactions topologies with one shower-like and one track-like object.

The particles are tracked through a cuboid detector filled with liquid argon and the dimensions in the (x, y, z) directions are $5 \text{ m} \times 5 \text{ m} \times 5 \text{ m}$, where z defines the beam direction, y is vertical and x is the drift direction. The simulation produces three-dimensional energy deposits within the detector volume that are converted into three images with height coming from the drift coordinate x and width from one-dimensional projections of the yz plane, similar to the three wire readout planes in the planned DUNE detectors [56]. These three views are referred to as u , v and w and are aligned at 35.9° , -35.9° and 0° to the vertical, respectively.

Three example events are shown in Fig. 1 with opening angles of 0° , 10° and 25° between the electron and muon, as seen in one of the three readout planes in the coordinates (wire, x). The shower-like activity in the events is shown in purple, and the track-like deposits are shown in magenta.

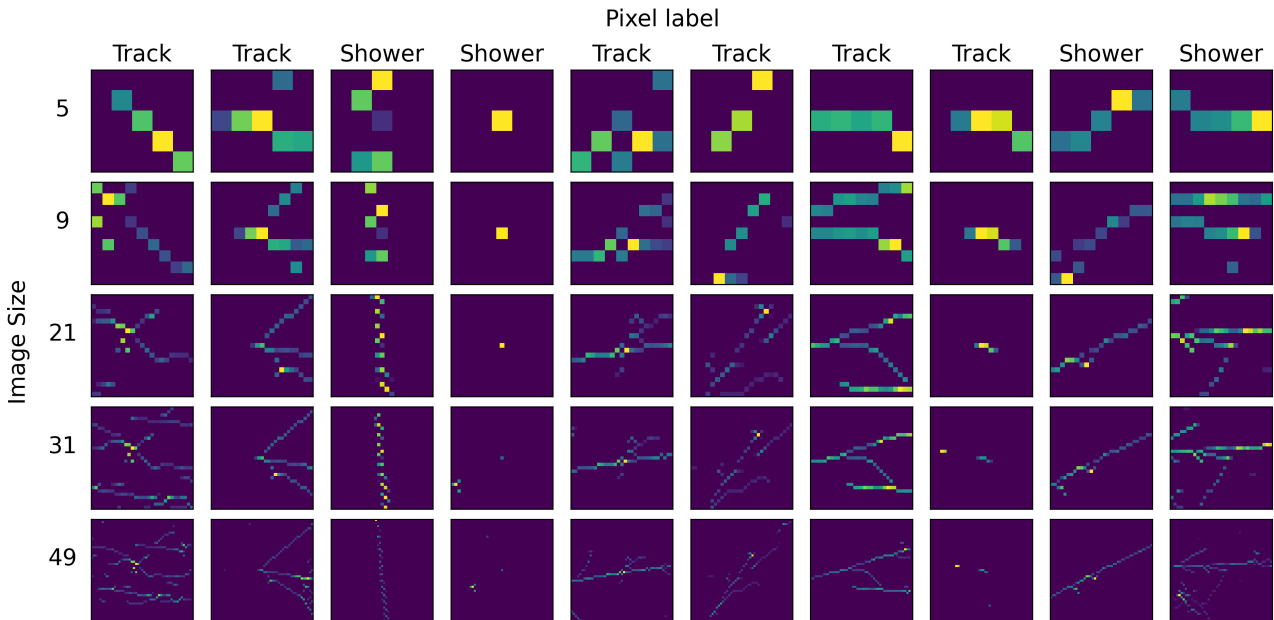


Fig. 2 Example event patches at various image sizes, categorized by pixel-level track and shower labels. Each row corresponds to a fixed patch size (given in pixels on the left), while each column shows the same event at different patch size scales. The label is determined by the classification of the central pixel as either track-like or shower-like.

It is clear that as the opening angle increases, the amount of overlap between the track- and shower-like energy deposits decreases.

4 Model design concepts

The models used in this study are all based on Convolutional Neural Network (CNN) architectures, which have achieved remarkable success in computer vision and beyond. CNNs form the backbone of historic architectures such as AlexNet (2012) [57], ResNet (2015) [58] and UNet (2015) [59]. They also play a key role in modern generative models, such as Stable Diffusion (2022) [60]. The convolutional layer uses a sliding filter which processes local windows of an image, sharing the same weights for all windows. This way it can effectively extract crucial features from the image. Given that LArTPC events can be interpreted as a collection of images, as described in Section 3, CNNs are naturally suited for their analysis. Numerous existing studies have successfully applied CNNs to LArTPC data [1, 2, 21, 24, 26, 61, 62].

One of the main properties of a convolutional layer is translation equivariance; the property of “respecting” translation symmetries of the input data. Section 4.1 explores this property in more detail and discusses how convolutions can be extended to respect symmetries beyond translation.

In this study, quantum circuits are introduced as replacements for specific components of a standard CNN architecture, resulting in a quanvolutional network. The quanvolutional layer, detailed in Section 4.2, modifies classical convolution while inheriting the symmetries of any convolutional layer. After a series of convolutional or quanvolutional operations, the generated feature maps are passed to a classifier, which may be either classical (a multi-layer perceptron (MLP)) or quantum (a parametrised quantum circuit (PQC)). Section 4.3 discusses the use of an equivariant quantum classifier for this task. Pooling layers may be introduced when dimensionality reduction is needed (See Figure 3).

4.1 Convolution and its equivariance

Equivariance is a property of a map $\mathcal{M} : X \rightarrow Y$ between two spaces (formally, G-sets) satisfied when [63]:

$$\mathcal{M}(gx) = g\mathcal{M}(x) \quad \forall g \in G, \forall x \in X. \quad (1)$$

This can be interpreted as: acting with a group element before acting with the map results in the same object in Y as first mapping to Y and then acting with the group element (See Fig. 4).

The convolution layers of a CNN are translation-equivariant maps. This means that if the original input becomes shifted, the output

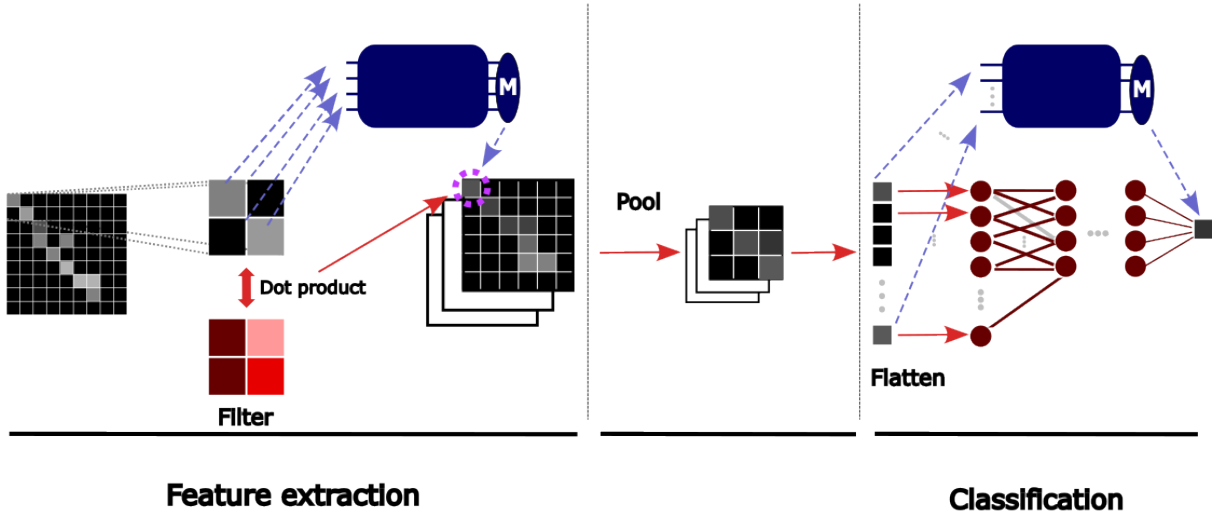


Fig. 3 A convolutional neural network and its extension to a quanvolution network. Data (greyscale) can be processed classically (red) or using quantum circuits (blue) where indicated. Quantum circuits can be used as a replacement for dot products with classical filters or classical classifier networks.

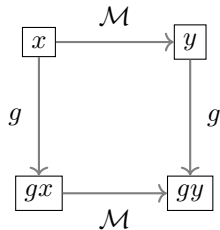


Fig. 4 Equivariant map \mathcal{M} and an element g of a group G acting on elements x, y of two spaces X, Y , respectively.

of the layer will be shifted accordingly. Mathematically, a convolution¹ can be expressed as [64, 65]:

$$[F \star W](g) = \sum_{h \in G} W(g^{-1}h)F(h), \quad (2)$$

where $g \in G_{out}$ are elements of the group the output is defined over, $h \in G$ are the elements of the group the input is defined over (can be different to G_{out}), W is the filter and F is the feature map (original data point in the case of the first convolution layer). Having defined the convolution this way, we can express the most common 2-D convolution by taking $G = G_{out} = (\mathbb{Z}^2, +)$, the (pixelised) translation group.

¹Technically, this is a closely related function called cross-correlation, but the term convolution is prevalent in ML literature.

For tasks dealing with images, of interest are convolutions defined over roto-translation groups; subgroups of the Euclidean group $E(2)$ [66]. The Euclidean group can be expressed as a semidirect product (See Appendix B) of the translation group $(\mathbb{R}^2, +)$ and the orthogonal group $O(2)$ which includes all continuous translations and reflections.

For this study, we shrink the $O(2)$ group to just the C_4 group (the four 90° rotations) for simplicity. The group convolution over our total group $(\mathbb{Z}^2, +) \rtimes C_4$ is visualised in Appendix B.

We note that this is the first investigation into the use of Euclidean symmetries on LArTPC images.

4.2 Quanvolution

The quanvolutional neural network has been proposed in [67] and [68] as a quantum-enhanced extension to the convolutional neural network.

We first note a common misinterpretation of the quanvolution: this architecture is often presented as using quantum circuits as “quantum filters”² performing a convolution [31, 67–69]. Appendix A shows that this interpretation is misleading and highlights a more subtle but crucial

²A convolution filter is often also referred to as a *kernel*.

relationship between the quanvolution and convolution. This new interpretation can be used to show how quanvolutions obtain their equivariance property. For completeness, the Appendix also briefly mentions how one could implement a version of the quanvolution which indeed uses the quantum circuit to produce the filter in an otherwise classical convolution. A study comparing performance of the two implementations could be an avenue for future research.

The quanvolution layer takes, as input, a feature map F . Windows of the feature map (like those in a convolution) are embedded in a unitary $U_{F,W}$ on the Hilbert space of a PQC. The number of qubits n_Q used is ordinarily equal to the number of pixels in the window. The full circuit processes the pixels contained in the window and returns a real number as output. This is ordinarily obtained via an expectation value of a chosen observable M . This real number is used to define the feature map of the following layer. The feature extraction part of Fig 3 represents this visually. In this work, the quanvolution circuits used are reuploader circuits of the form:

$$F_{out}(g) = \langle \psi_0 | (U_{\theta}^{\dagger} U_{F,W}^{\dagger}(g))^R | M | (U_{\theta} U_{F,W}(g))^R | \psi_0 \rangle, \quad (3)$$

where $|\psi_0\rangle$ is some initial state of the qubits, taken in this study to be the $|0\rangle^{\otimes n_Q}$, U_{θ} is an ansatz - a unitary with trainable parameters and R is the number of times the $U_{\theta} U_{F,W}(g)$ -block is repeated. A general circuit of this kind is pictured in Figure 5.

$U_{F,W}$ used was the rotation embedding

$$U_{F,W}(g) = \bigotimes_{i \in [n_Q]} RX_i(F_{W(g),i}), \quad (4)$$

with RP denoting a Pauli P rotation and $F_{W(g),i}$ being the value of the feature map assigned to qubit i in the window of g . U_{θ} was a nearest-neighbour entangling ansatz with two trainable parameters per qubit, per entanglement block layer,

$$U_{\theta} = \bigotimes_{l \in [L]} RZ_{n_Q}(\theta_{2,l,n_Q}) RY_{n_Q}(\theta_{1,l,n_Q}) \bigotimes_{i \in [n_Q-1]} CX_{i,i+1} RZ_i(\theta_{2,l,i}) RY_i(\theta_{1,l,i}), \quad (5)$$

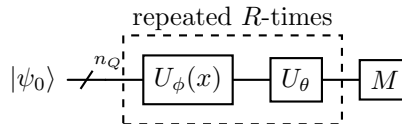


Fig. 5 General n_Q -qubit reuploader circuit architecture used for all circuits in this work. $U_{\phi}(x)$ is a data-encoding unitary for a datapoint x . U_{θ} is a trainable ansatz which does not depend on data. M denotes a chosen measurement unitary whose expectation value is used as the output of the trainable circuit. Exact choices for $U_{\phi}(x)$, U_{θ} , M are discussed in the relevant sections of the text.

where L is a hyperparameter (See Table C). An example circuit diagram can be found in Appendix C.

A G -equivariant quanvolution can be achieved in analogy to the standard quanvolution. That is, every dot product between a feature map and a filter of the equivariant convolution described in 4.1 is replaced with a pass of the feature map through a quantum circuit, as described earlier in this Section. We note that the equivariance of this layer comes purely from its classical construction and the use of identical circuit structure for each group element g . Appendix A shows how a quanvolution inherits its equivariance from a convolution. In other words, the individual circuits used do not need to be equivariant maps. This is unlike what will be discussed in Section 4.3, where the invariant quantum classifier is constructed using methods from geometric quantum machine learning.

As mentioned earlier, it is customary to use quanvolution circuits with the same number of qubits as the number of pixels in the sliding window of the quanvolution. There is, however, no need to adhere to this restriction. As long as the quanvolution circuits used depend on a given group element solely via their embedding, any size circuit can be used. Growing the circuit to many tens of qubits will likely be necessary for it to be intractable classically.

Additionally, whilst small filter sizes are commonly used in CNNs, some notable results from the literature show that large filters can achieve competitive performance [70, 71]. Future studies should investigate increasing the size of the sliding window in quanvolutions. Depending on the ansatz used, this could quickly become intractable to known classical simulation techniques.

4.3 Invariant quantum classifier

Geometric quantum learning has bloomed in the recent years. Theoretical results show that some geometric models have desirable properties [72] and have been proposed as a strong candidate for potential quantum speedup [35]. Given a group, finding an equivariant ansatz can be performed in a variety of ways [46]. A quantum classifier acting on classical data can be made *invariant* if the embedding, the ansatz and the measurement are equivariant [45, 46].

The classifier circuits take as input the last layer of the feature extraction part of the network. Preserving rotation equivariance between the two parts of the network can be ensured by averaging along the C_4 dimension as well as along the regular convolution channels, resulting in a single image representing all the information contained in the last feature extraction layer. Other schemes for this procedure might be possible and could be explored in the future.

The invariant circuits used as classifiers in the study also follow the general structure of Figure 5. $U_\phi(x)$ is chosen to be the rotation embedding $U_\phi(x) = \bigotimes_i RX_i(x_i)$, with $i \in [n_Q]$ and RX being a Pauli X rotation gate. This embedding is equivariant to C_4 rotations. The ansatz U_θ is constructed using equivariant gates according to a scheme detailed in Appendix D and M is a Z -basis measurement of the central qubit, also equivariant to C_4 .

Given the ansatz and hyperparameters used, the number of parameters in this layer is much smaller (on the order of 10) than those used by the MLPs of the other models.

5 Model architectures

This section details how the concepts from the previous Section have been combined to design the specific architectures used on the LArTPC datasets.

We consider the CNN to be made up of two modules: the feature extraction module (with optional pooling after each layer) and the classification module. To help keep track of the different variants of the models, we refer to them by the symmetry (equivariance) status S and type T of their modules, where $S \in \{E, NE\}$ and $T \in \{Q, C\}$. E denotes ‘equivariant’, NE -

‘non-equivariant’, Q - ‘quantum’, C - ‘classical’. Together, a given architecture can be referred to as $TS \rightarrow TS$. Table 1 details all the models used.

Feature extraction	Classification	#parameters
NEC	NEC	10^5
NEC	NEC	10^3
NEQ	NEC	10^3
EC	NEC	10^5
EQ	NEC	10^3
EQ	EQ	10^2

Table 1 Summary of the architectures used in the study using the nomenclature introduced in the text. Number of parameters is given as an order of magnitude estimate as the choice of hyperparameters impacts the exact number. Top three models have no symmetries beyond translations. The remaining are equivariant to C_4 rotations at least in the feature extraction part.

5.1 Classical benchmarks

Three classical benchmark models are used in this study:

- **Deep CNN** ($CNE \rightarrow CNE$) - A six-layer convolutional neural network with 3×3 filters and output channels [16, 16, 32, 32, 64, 64], in each layer respectively.
- **Small CNN** ($CNE \rightarrow CNE$) - A compact convolutional network with 2 layers of 2×2 filters and three output channels per layer.
- **Equivariant Deep CNN** ($CE \rightarrow CNE$) - A deep CNN that incorporates C_4 group convolutions, introducing rotational symmetry while maintaining the same overall architecture as the deep CNN.

All models use an MLP as the final classifier.

5.2 Quantum-enhanced architectures

Three quanvolutional networks with 2×2 quanvolution windows are implemented.

One is a standard quanvolutional network using operations described in Section 4.2 for feature extraction, followed by an MLP. The other two are symmetry-aware. Feature extraction in both is achieved with a C_4 -symmetric quanvolution described in 4.2. They differ only in their classifier module. The first uses a classical MLP and the other, a quantum, symmetry-aware classifier.

The second model is a fully *invariant* classifier, as discussed in 4.3. This means that two images which differ by a C_4 rotation will result in the same output, leading necessarily to the same label.

- **Standard quanvolutional NN** $QNE \rightarrow CNE$ – Two quanvolutional layers, each with three output channels, followed by a 2-layer MLP.
- **Partially symmetric quanvolutional NN** $QE \rightarrow CNE$ – Two C_4 -symmetric quanvolutional layers, each with three output channels. Classification with a 2-layer MLP.
- **Fully symmetric quanvolutional NN** $QE \rightarrow QE$ – Two C_4 -symmetric quanvolutional layers, each with three output channels. Classification with a C_4 -symmetric quantum classifier using an equivariant embedding, equivariant reuploader circuits and an equivariant measurement.

6 Results

6.1 Performance on the MicroBooNE open dataset

In this section, we evaluate the performance of our proposed models on the open MicroBooNE dataset. Specifically, we investigate how the spatial context surrounding a classified pixel influences the model’s performance. Figure 2 illustrates examples of the same pixel within an event as part of progressively larger patches.

In our framework, a patch refers to the local neighbourhood of a pixel that is provided as input to the model. While the model ultimately classifies only the central pixel (as either “track” or “shower”), it utilizes the surrounding information within the patch to make this determination. For instance, if a pixel lies within a straight, connected path and exhibits consistent energy signatures, the model is likely to classify it as part of a track.

Incorporating a larger field of view offers contextual information about the broader topology, aiding classification. However, excessively large patches may introduce unrelated or irrelevant structures, potentially degrading model performance by introducing noise. The optimal patch size for LArTPC pixel classification remains an open question. In this work, we contribute to this

ongoing investigation by evaluating model performance on the simplified MicroBooNE dataset described in Section 3.1.

Figure 6 presents the performance of the models described in Section 4 across different patch sizes.

Notably, larger models exhibit the ability to process increasingly large patches effectively—the more contextual information they receive, the better their classification performance. Conversely, smaller models demonstrate a decline in performance when presented with patches that are too large, likely due to an inability to process the additional information effectively. A patch size of 21 pixels appears to be an optimal choice for these models.

Quantum models demonstrate superior performance compared to their classical counterparts across multiple patch sizes when constrained to a similar number of trainable parameters and with an identical number of filters. A 100-fold increase in the number of parameters allows classical models to surpass the performance of the quantum-enhanced architectures.

The fully equivariant architecture (EQEQ) performs the worst at small patch sizes. The hardness of classifying these patches likely comes from the limited number of geometric arrangements of hits within a neighbourhood this small, often shared by both tracks and showers (Some examples can be seen in Figure 2)³. Introducing equivariance into the model architecture can enhance performance, as evidenced by the large classical models, though this effect depends on model expressiveness.

Our findings suggest that larger patch sizes require more expressive models to leverage the additional information effectively. Symmetry constraints can be beneficial, but only when the model is sufficiently expressive. If a model is too small, enforcing symmetry may hinder learning by diverting limited capacity away from representing complex features. Once a model reaches sufficient capacity, however, incorporating symmetry appears to be advantageous.

A key limitation of large-scale studies involving the simulation of quantum devices on classical

³As no padding was used throughout this study, deep models would reduce the size of their feature maps to 1×1 before the classification layer for small patch sizes. We thus only apply large models to patch sizes 21 and above.

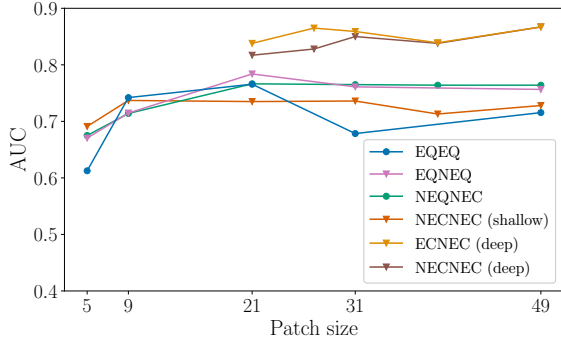


Fig. 6 Receiver operating characteristic area under curve (ROC AUC) for models used in this study with increasing pixel patch size.

hardware is the substantial computational cost in terms of time and RAM. In our study, performing hyperparameter optimization for selecting the best model (details in Appendix C) at each patch size (Figure 6) requires multiple days per patch size. This computational overhead imposes constraints on the volume of training data and number of filters that can be incorporated into the optimization process.

To further investigate the learning capabilities of our models, we analyse their performance as a function of training dataset size. Specifically, we evaluate the best-performing models from the hyperparameter optimization study across training set sizes ranging from 100 to 1000 data points, using the generally favourable patch size of 21. The metrics for each model are reported by averaging the 10 best-performing instances from a run, using hundreds of random seeds for each training size. We report the mean, standard deviation, and maximum performance. The primary goal of this study is to assess the extent to which models can generalize in a data-constrained setting.

The results of this experiment are presented in Figure 7. The overall trend reveals that the deep CNN with group convolutions (GCNN) consistently achieves the highest performance, followed by the deep CNN, then the quanvolutional NN, and finally the shallow CNN.

Several key observations can be made from these results. First, for 100 data points, the deep CNN and quanvolutional NN exhibit similar performance, suggesting that despite having far fewer feature maps, the quanvolutional NN extracts

representations of comparable quality to those learned by the deep CNN. However, under this limited data regime, the deep GCNN still outperforms all other models, a behaviour commonly observed in architectures with strong inductive biases—a property that appears evident in this study as well.

As the training set size increases, the performance gap between the deep CNN and the quanvolutional NN widens. While the GCNN remains the most performant of them all though the performance gap narrows between it and the deep CNN. This indicates that as more data becomes available, the deeper classical architecture can refine its representations more effectively to align closer to the GCNN. Additionally, the greater performance of the quanvolutional NN compared to the shallow CNN suggests that the representations learned by the quanvolutional NN are richer and more informative, enabling better feature extraction for the final classification layers. A trend that remains even as we increase the amount of training data.

These findings underscore the importance of both model architecture and inductive biases in data-limited scenarios. Models with strong symmetry constraints such as the GCNN demonstrate superior generalization when data is scarce, whereas architectures with weaker biases, such as the deep CNN, benefit more from increased data availability. The performance of the quanvolutional NN suggests that quantum-inspired architectures may offer competitive feature representations despite their reduced parameter count. However, further investigations into their scalability with larger datasets are warranted.

6.2 Performance on the neutrino-like dataset

As described in Section 3.2, events in this dataset are characterized by a simple yet informative parameter—the angle between the two created particles. This angle serves as a proxy for the classification difficulty of individual pixels: smaller angles correspond to more challenging classification tasks due to increased spatial overlap and denser regions of energy deposition.

Understanding how models perform in high-density regions is crucial for future LArTPC experiments, as these regions present a major

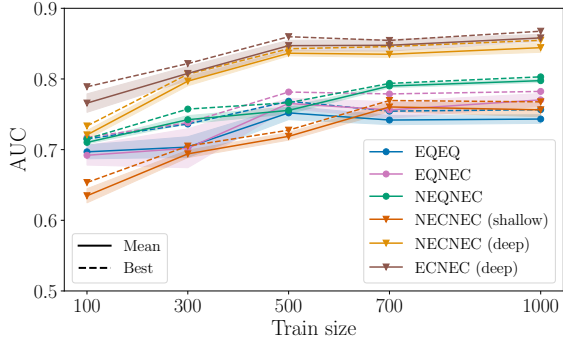


Fig. 7 Learning capability of models used in this study. Vertical axis is the receiver operating characteristic area under curve (ROC AUC) and the horizontal axis is a training size (number of patches). Patch size was kept at 21.

bottleneck for accurate event reconstruction. To systematically investigate how model performance scales with complexity, we divide the dataset into three categories based on the inter-particle angle:

- **Easy:** $15^\circ - 180^\circ$ (widely separated particles)
- **Medium:** $5^\circ - 15^\circ$ (moderate overlap)
- **Hard:** $0^\circ - 5^\circ$ (significant overlap and the most complex topology)

The performance of the models across these three categories is summarized in Figure 8. A clear pattern emerges when comparing the shallow CNN to the quantum NN: while the quantum NN consistently outperforms the shallow CNN across all levels of difficulty, the largest performance gap appears in the hardest category ($0^\circ - 5^\circ$). This suggests that the quantum NN is better equipped to resolve complex topologies and extract meaningful features, a crucial property when dealing with busy detector regions. We can potentially attribute this to the richer feature maps produced by the quantum NN.

However, we also observe that larger classical CNNs—with significantly more filters and overall capacity—continue to outperform the quantum NN across all difficulty levels. Interestingly, separation between the equivariant and non-equivariant models disappears when tested on this dataset. In fact, non-equivariant models, in general, prevail. Whilst each of the events in this dataset has a sense of direction (most patches will have structures oriented along the direction of the muon), which could render the addition of symmetries unhelpful, the patches used for training

and testing are sampled from 100 different events, where that direction is isotropic.

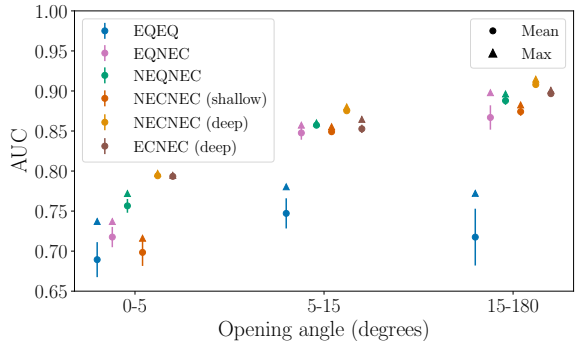


Fig. 8 Learning capability of models used in this study. Vertical axis is the receiver operating characteristic area under curve (ROC AUC) and the horizontal axis is the opening angle between the electron and muon particles. The patch size was kept at 21.

7 Conclusion

This paper contributes to the fields of experimental neutrino physics and quantum machine learning. In the context of particle physics, we address crucial open questions in ML-driven pixel-level LArTPC classification. We examine the effects of patch size on the performance of the models, the benefits of including rotational symmetries in their design and begin to study their behaviour in dense environments. In the quantum machine learning domain, we point out a common misconception about a popular model, define it in a rigorous way based on its connection to the convolution layer, and show, for the first time, how to design it such that it respects symmetries beyond translation.

Results show that quantum-enhanced models are competitive with fully classical ones. For a similar number of parameters, quantum models consistently achieve better results. They remain outperformed by classical models with 10 times more parameters, however. This trend holds for all the analyses implemented within this work.

Using the MicroBooNE data, it has been shown that large models can utilise large patches for pixel classification, whilst the amount of information contained in these large patches becomes confusing for smaller models. These find optimal

performance at a patch size of 21. An obvious question follows: can the large models benefit from even larger patches?

One downside of our study is that we operate in a very low-data regime, showing results for models trained on up to only 1000 samples. Given the amount of data available in LArTPC experiments and HEP experiments in general, the use of more efficient QML pipeline techniques becomes paramount. Future studies should strive to reduce the computational training and test time by leveraging GPUs, just-in-time compilation or simulations beyond state-vector-methods.

Implementing a custom “neutrino-like” dataset, we defined a single parameter (angle between the two produced particles) as a proxy to denote the difficulty of classifying patches from a given event. Recognising a similar way to categorise pixels in actual experiments could become a highly beneficial analysis tool of the implemented classifiers.

The inclusion of C_4 symmetry in the models does not guarantee a substantial advantage. No advantage is seen within the (small) quanvolution models - the non-symmetric quanvolution performs best in almost all scenarios. A small advantage of the (large) symmetric classical model over its non-symmetric counterpart can be seen in the MicroBooNE dataset but not in the neutrino-like dataset. A study varying the symmetry group (adding reflections, probing C_n with $n \neq 4$, or going to the continuous $SO(2)$ regime) is needed to determine which (if any) provides the best inductive bias for models dealing with LArTPC images. The case for discrete groups in quanvolutions can be explored using methods described in this work.

An obvious direction for future study is an extension to larger subgroups of the Euclidean group. We note also that some potentially interesting combinations of the feature extraction and classification modules have not been explored. Namely, $EC \rightarrow EC$, $EQ \rightarrow EC$ and $EC \rightarrow EQ$. These would be fully invariant classifiers. Contrasting the properties and performance of all the combinations of the feature extraction and classification modules could further our understanding of any potential advantages offered by quantum elements in the architecture, as well as the inclusion of symmetry in the model.

Acknowledgements. MJ thanks Peter T J Bradshaw for the valuable discussions. We acknowledge the MicroBooNE Collaboration for making publicly available the data sets [52] employed in this work. These data sets consist of simulated neutrino interactions from the Booster Neutrino Beamline overlaid on top of cosmic data collected with the MicroBooNE detector [2].

Appendix A The misinterpreted quanvolution

As hinted at in Section 4, the quanvolution layer used in this study does not - contrary to common interpretation - implement a quantum circuit as a “filter” in an otherwise classical convolution.

Recalling Equation 2, we note that the convolution involves a dot product of two functions defined on a common space of group elements, where one of the functions is “moved” through that space.

In order for the quantum circuit to act as the filter, it would have to be defined on the pixels of the feature map [65]. One should be able to ask “What is the value of the quantum circuit at pixel $(2, 2)$?”. From the construction of the quanvolution defined in the paper it is clear that such question is meaningless without first finding the value of the feature map at that point - the “value of the circuit” is necessarily defined through the feature map which becomes embedded into it.

One *can* think of the quantum circuit as a filter in the image-processing sense, a predefined operation applied to a neighbourhood of a pixel [73]. This should not, however, be extended to thinking of the circuit as the filter of a convolution, based on the above argument.

A.1 Where is the convolution?

As reasoned above, the circuit itself cannot be thought of as a filter in a convolution. The quanvolution, however *feels* like a convolution; it seems to inherit its equivariance property, has a stride, a window size and can be implemented, algorithmically, in a similar way to a convolution. It also, as shown in the main text, seems to very naturally extend to group-quanvolutions based on group-convolutions. One way of understanding the connection between the two is to consider how

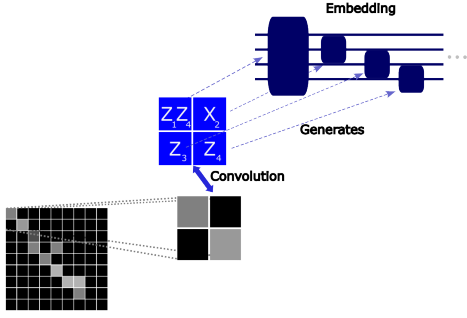


Fig. A1 The embedding unitary pictured as a convolution with a Hermitian-matrix-valued filter.

the feature map of a layer is embedded into the quantum circuit.

Let us consider a convolution filter W which is *matrix-valued*. Observe now that if these matrices $W(g)$ are restricted to being Hermitian and commuting with each other, the embedding can be expressed as:

$$\begin{aligned} U_{F,W}(g) &= \exp\left(-i \sum_h F(h)W(g^{-1}h)\right) \quad (\text{A1}) \\ &= \exp(-i [F \star W](g)). \end{aligned}$$

The embedding circuit is *generated* by a convolution between the feature map F and a “quantum filter” W . Figure A1 demonstrates this idea. The simple rotation embedding used in the main text (Equation 4) can be achieved with a filter containing one of the $\{X_i \mid i \in [n_Q]\}$ gates at each entry.

With Equation A1, the quanvolution operation can be written as:

$$\begin{aligned} [F \star^Q W](g) &= \text{Circ}(U_{F,W}(g)) \\ &= \text{Circ}(\exp(-i [F \star W](g))), \end{aligned} \quad (\text{A2})$$

where the $\text{Circ}(U(g))$ function obtains a real-valued property of a state which depends on g only through $U_{F,W}(g)$. An example would be a reuploader circuit utilising expectation values, like the one used in the main text:

$$\begin{aligned} \text{Circ}(U_{F,W}(g)) &= \\ &= \langle \psi_0 | (U_\theta^\dagger U_{F,W}^\dagger(g))^R | M | (U_\theta U_{F,W}(g))^R | \psi_0 \rangle. \end{aligned} \quad (\text{A3})$$

An example of a circuit which does not satisfy the above constraint would be:

$$\begin{aligned} \text{Circ}(U_{F,W}(g)) &= \\ &= \langle \psi_0 | (U_\theta^\dagger U_{F,W}^\dagger(g))^R | M_g | (U_\theta U_{F,W}(g))^R | \psi_0 \rangle, \end{aligned} \quad (\text{A4})$$

where the observable M depends on the position in the produced feature map.

To illustrate how the quanvolution inherits the equivariance property from a convolution without being a convolution itself, let us begin with an important property of feature maps in G -convolutions:

$$gF(x) = F(g^{-1}x). \quad (\text{A5})$$

This simply states that to access a value of the g -transformed feature map one can look up that value in the original feature map at the point which transforms to x via g . Now, we show a well-known proof for the equivariance of a G -convolution:

$$\begin{aligned} [uF \star W](g) &= \sum_{h \in G} F(u^{-1}h)W(g^{-1}h), \quad (h \rightarrow uh) \\ &= \sum_{h \in G} F(h)W(g^{-1}uh) \\ &= \sum_{h \in G} F(h)W((u^{-1}g)^{-1}h) \\ &= [F \star W](u^{-1}g) \\ &= u [F \star W](g), \end{aligned} \quad (\text{A6})$$

where the last line holds as the convolution defines a new feature map.

Now for a quanvolution:

$$\begin{aligned} [uF \star^Q W](g) &= \text{Circ}(U_{uF,W}(g)) \\ &= \text{Circ}(\exp(-i [uF \star W](g))) \\ &= \text{Circ}(\exp(-i [F \star W](u^{-1}g))) \\ &= [F \star^Q W](u^{-1}g) \\ &= u [F \star^Q W](g), \end{aligned} \quad (\text{A7})$$

where the third line comes from A6, and again in the last line, we used the property of feature maps

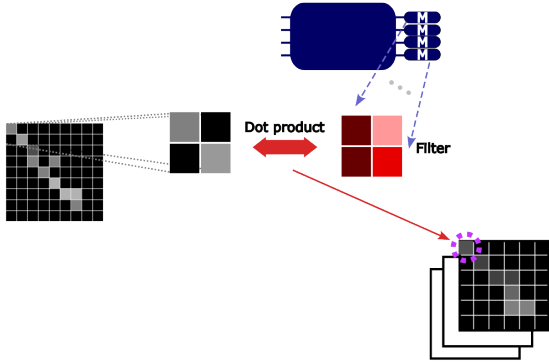


Fig. A2 Proposed convolution with a quantum-enhanced filter. The circuit consists only of an ansatz, and no data embedding is present.

(A5). This illustrates how any G -quantum convolution can be obtained from an appropriate G -convolution and explains why the proposed C_4 -quantum convolution works.

For completeness, having seen that the quantum convolution is itself not a convolution (though closely related), we briefly present one way of obtaining a "quantum-enhanced", classical convolution.

In the proposed scenario, a parametrised quantum circuit which does not take data as input (no data embedding present) and consists only of an ansatz is used. A set of measurements is performed, e.g., one on each qubit of the circuit, resulting in a scalar-valued, classical filter. Then, a standard convolution is performed. This is illustrated in A2.

Appendix B Group-convolution visualised

This section contains visualisation of the standard (Fig. B3) as well as the first (B4) and subsequent (B5) layers of the $Z_2 \times C_4$ convolution.

To understand how a group convolution is performed, one simply needs to recognise the elements of the groups in Equation 2 in the input and output layers of the convolution. We refer to these as G and G_{out} , respectively. The feature map is accessed only at $h \in G$, meaning that we simply need to find the correct group element and "read off" the value of the feature map at that element. For the filter we do the same, but we first need to consider how elements of G_{out} act on G .

For a standard convolution (See Figure B3), both the input and output layers are defined over

$(Z_2, +)$. The elements $g^{-1}h$, at which the filter is accessed are just shifted locations on the 2-D grid.

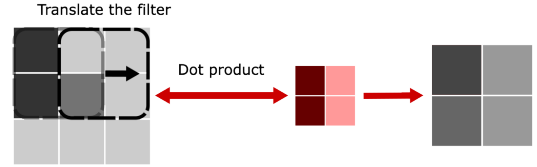


Fig. B3 A schematic of a standard convolution. The filter (red) "slides" over the feature map and dot products between windows of the feature map and the filter are taken to produce next layer's feature map.

In Figure B4, a first-layer $(Z_2, +) \times C_4$ -convolution is shown. Here, the input layer is still defined only over $(Z_2, +)$, but the output exists in $(Z_2, +) \times C_4$. Elements of this group can be expressed as $g = tr$, where t contains the translation and r corresponds to the rotation part of the group. $g \in G$ now has two effects on the members of $(Z_2, +)$; the t element of g corresponds to shifting points on the grid (so for all t , $g = te$ corresponds to the usual convolution) whilst the r element rotates the 2-D plane. The following layer will have 4 elements, each corresponding to one of the rotations of the C_4 group. This can be thought of as the feature map containing a 4-element vector at each pixel. This vector is in the *regular* representation of the C_4 group. This means that acting on it with a group element simply permutes the components of the vector [66].

Finally, what happens when both the input image as well as the convolution are defined over the compound group $(Z_2, +) \times C_4$? Again, we think about the action of $g = tr$, but this time it acts on members of its own group, $h = t'r'$. The t component, as previously, only translates within a given 2-D plane. The r component now performs both the rotation of the 2-D plane ($r^{-1}t'$) as well as the permutation of the vectors in the regular representation of C_4 ($r^{-1}r'$).

We note the obvious asymmetry in the two elements of the group; t acts only on t' , whereas g acts on both g' and t' . This is a consequence of using the semidirect product to construct the group [74]. Without this property, our group would not be able to capture the rotations of the pixel plane we are interested in.

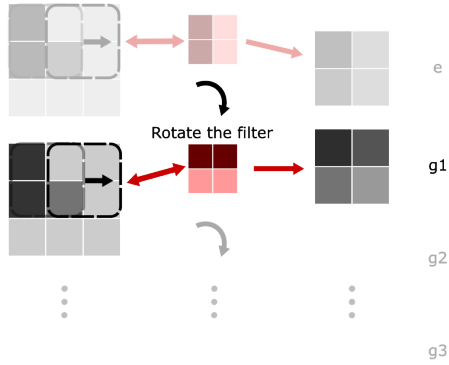


Fig. B4 A schematic of the first layer of a $(\mathbb{Z}^2, +) \times C_4$ convolution. The filter is acted on with the group action (rotations and translations) to produce the second layer feature map which is now a vector with four components at each pixel. Each component corresponds to a rotation of the filter.

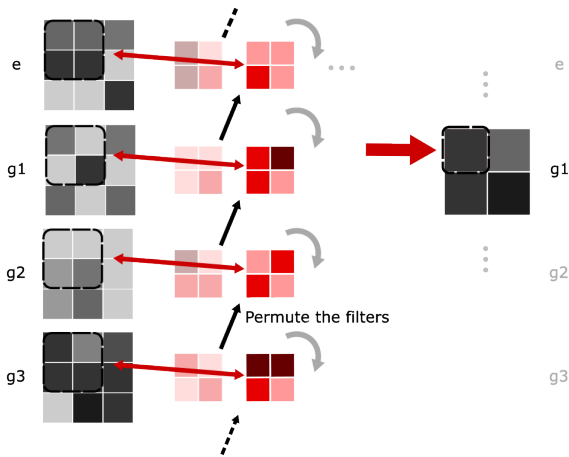


Fig. B5 A schematic of the second (or subsequent) layer of a $(\mathbb{Z}^2, +) \times C_4$ convolution. Figure shows how one of the pixels in one of the vector components of the output layer is obtained. The pixel contains dot products of all the elements of the input layer with the elements of the filter. The filter's elements undergo rotation in the \mathbb{Z}^2 space as well as permutation in the C_4 space.

Appendix C Details of hyperparameter optimisation

For training and hyperparameter optimisation, `ray` [75] and `weightsandbiases` (`wandb`) [76] packages were used extensively.

In the patch size study, for each of the patch sizes, a hyperparameter search over around 200

models per architecture has been performed. Models were allowed to train for up to 100 epochs but were often cut short by the `RayScheduler` object used in the pipeline. The `RayScheduler` class contains methods for speeding up wide model searches by cutting jobs short based on a metric of choice. For this study, models were terminated based on the loss they achieved during training.

Loss, validation loss and validation accuracy were reported throughout training to online and local `wandb` project directories, which helped with visual assessing of their performance and accessing trained models. After training, the model used for testing was chosen based on the highest validation accuracy achieved during training.

The ansatz described in Equation 5 is pictured in Figure C6.

Appendix D Details of the quantum geometric classifier

The geometric classifier circuits are invariant to rotations of the feature maps received by them (coming from the last layer of the quanvolution and potential pooling). These classifier circuits, for ease of software implementation, were defined only on 9-qubit circuits. That means that only 3×3 patches could be classified. This provided a restriction for the feature extraction layers (See Figure 3) preceding the quantum classifier. That is, the combination of the quanvolutions and the classical pooling had to result in a final layer that has a shape 3×3 (before being flattened).

The invariant classifiers' layers have been obtained according to the following protocol:

- randomly pick a number N_1 of single-qubit gates (See Table C) (e.g. 1)
- randomly pick a number N_2 of two-qubit gates (See Table C) (e.g. 1)
- randomly pick a qubit for each of the 1-qubit gates to act on (e.g. qubit 3)
- randomly pick a pair of qubits for each of the 2-qubit gates to act on (e.g. qubits 3 and 6).
- for each of the gates, randomly choose a Pauli string of the correct length (e.g. X , XY), creating generators (X_3, X_3Y_6)

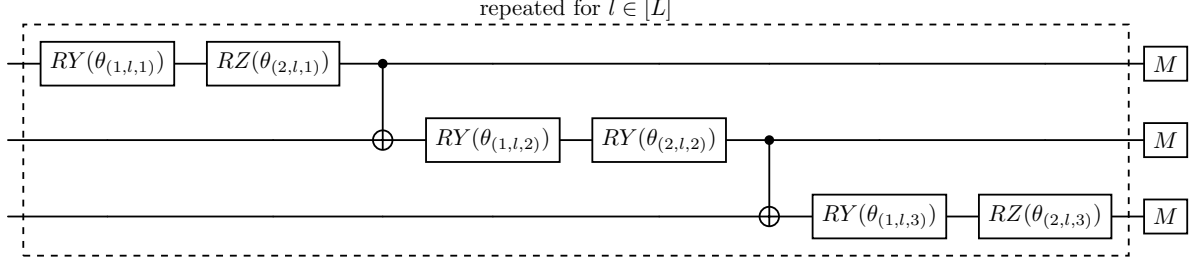


Fig. C6 A 3-qubit example of the ansatz in quanvolution circuits used in this study.

Hyperparameter	Sampled set	Models
Learning rate	$[10^{-3}, 10^{-1}]$	All
number of layers (quanvolution circuits)	$\{1, 2\}$	EQNEC, EQEQ, NEQNEC
number of filters (quanvolution)	$\{1, 2, 3\}$	EQNEC, EQEQ, NEQNEC
number of reuploads (quanvolution circuits)	$\{1, 2\}$	EQNEC, EQEQ, NEQNEC
maximum for parameter initialisation (quanvolution circuits)	$\{10^{-3}, 10^{-1}, \frac{\pi}{4}, \frac{\pi}{2}, 2\pi\}$	EQNEC, EQEQ, NEQNEC
dense units sizes	$\{(8, 8), (128, 32)\}$	EQNEC, NEQNEC
use of dropout	$\{\text{True}, \text{False}\}$	EQNEC, NEQNEC
dropout amount	$\{10^{-4}, 0.5\}$	EQNEC, NEQNEC
classifier number of layers	$\{1, 2, 3, 4\}$	EQEQ
classifier number of reuploads	$\{1, 2, 3\}$	EQEQ
number of 1-local gates	$\{1, 2, 3, 4\}$	EQEQ
number of 2-local gates	$\{1, 2, 3, 4\}$	EQEQ
placement of 1-local gates	See Appendix D	EQEQ
placement of 2-local gates	See Appendix D	EQEQ

Table C1 Hyperparameters optimised for the models used in the study. $[]$ signifies a continuous range and $\{\}$ a discrete set.

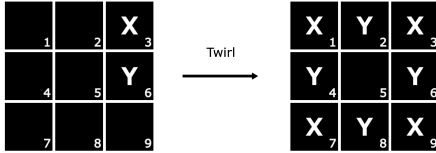


Fig. D7 A C_4 -invariant gate obtained from twirling X_3Y_6 overlaid on a pixelised grid representing the input layer to the classifier defined in the text.

- by twirling the generators, obtain generators of C_4 -equivariant gates ($X_1+X_3+X_5+X_7$, $X_3Y_6+X_1Y_0+X_5Y_2+X_7Y_8$)
- reject the choice if the resulting generators cannot be implemented as combinations of 2-local gates, accept otherwise

The rejection criterion in the last step refers to a situation like:

$$\tau(X_0Z_2) = X_0Z_2 + X_2Z_8 + X_8Z_6 + X_6Z_0. \quad (\text{D8})$$

Because the elements of this generator do not commute, the resulting parametrised gate cannot be implemented as a product of 2-qubit gates, $e^{i\theta\tau(X_0Z_2)} \neq e^{i\theta X_0Z_2} e^{i\theta X_2Z_8} e^{i\theta X_8Z_6} e^{i\theta X_6Z_0}$.

We note a detailed study of rotation-invariant circuits for images in [77], where the feature extraction is achieved using equivariant convolutions (our work uses equivariant quanvolutions).

References

- [1] Abratenko, P., *et al.*: Search for an anomalous excess of charged-current quasielastic ν_e interactions with the

- MicroBooNE experiment using Deep-Learning-based reconstruction. *Phys. Rev. D* **105**(11), 112003 (2022) <https://doi.org/10.1103/PhysRevD.105.112003> [arXiv:2110.14080](https://arxiv.org/abs/2110.14080) [hep-ex]
- [2] Acciarri, R., *et al.*: Convolutional neural networks applied to neutrino events in a liquid argon time projection chamber. *Journal of Instrumentation* **12**(03), 03011 (2017) <https://doi.org/10.1088/1748-0221/12/03/P03011>
- [3] Argüelles, C.â., Esteban, I., Hostert, M., Kelly, K.â., Kopp, J., Machado, P.â.â., Martinez-Soler, I., Perez-Gonzalez, Y.â.: Microboone and the ν_e interpretation of the miniboone low-energy excess. *Physical Review Letters* **128**(24) (2022) <https://doi.org/10.1103/physrevlett.128.241802>
- [4] Machado, P.A.N., Palamara, O., Schmitz, D.W.: The short-baseline neutrino program at fermilab. *Annual Review of Nuclear and Particle Science* **69**(1), 363–387 (2019) <https://doi.org/10.1146/annurev-nucl-101917-020949>
- [5] Abi, B., *et al.*: Long-baseline neutrino oscillation physics potential of the DUNE experiment. *Eur. Phys. J. C* **80**(10), 978 (2020) <https://doi.org/10.1140/epjc/s10052-020-08456-z> [arXiv:2006.16043](https://arxiv.org/abs/2006.16043) [hep-ex]
- [6] Fukasawa, S., Ghosh, M., Yasuda, O.: Complementarity Between Hyperkamiokande and DUNE in Determining Neutrino Oscillation Parameters. *Nucl. Phys. B* **918**, 337–357 (2017) <https://doi.org/10.1016/j.nuclphysb.2017.02.008> [arXiv:1607.03758](https://arxiv.org/abs/1607.03758) [hep-ph]
- [7] Brahma, B., Giri, A.: Probing Dual NSI and CP Violation in DUNE and T2HK (2023). <https://arxiv.org/abs/2306.05258>
- [8] Müller, K., Suliga, A.M., Tamborra, I., Denton, P.B.: Measuring the supernova unknowns at the next-generation neutrino telescopes through the diffuse neutrino background. *Journal of Cosmology and Astroparticle Physics* **2018**(05), 066–066 (2018) <https://doi.org/10.1088/1475-7516/2018/05/066>
- [9] Domingo, F., Dreiner, H.K., Kähler, D., Nangia, S., Shah, A.: A Novel Proton Decay Signature at DUNE, JUNO, and Hyper-K (2024). <https://arxiv.org/abs/2403.18502>
- [10] Baller, B.: Liquid argon tpc signal formation, signal processing and reconstruction techniques. *Journal of Instrumentation* **12**(07), 07010–07010 (2017) <https://doi.org/10.1088/1748-0221/12/07/p07010>
- [11] Collaboration, I.: ICARUS at the Fermilab Short-Baseline Neutrino Program – Initial Operation (2023). <https://arxiv.org/abs/2301.08634>
- [12] Acciarri, R., *et al.*: Design and Construction of the MicroBooNE Detector. *JINST* **12**(02), 02017 (2017) <https://doi.org/10.1088/1748-0221/12/02/P02017> [arXiv:1612.05824](https://arxiv.org/abs/1612.05824) [physics.ins-det]
- [13] Abi, B., *et al.*: First results on ProtoDUNE-SP liquid argon time projection chamber performance from a beam test at the CERN Neutrino Platform. *JINST* **15**(12), 12004 (2020) <https://doi.org/10.1088/1748-0221/15/12/P12004> [arXiv:2007.06722](https://arxiv.org/abs/2007.06722) [physics.ins-det]
- [14] Acciarri, R., *et al.*: Construction of precision wire readout planes for the Short-Baseline Near Detector (SBND). *JINST* **15**(06), 06033 (2020) <https://doi.org/10.1088/1748-0221/15/06/P06033> [arXiv:2002.08424](https://arxiv.org/abs/2002.08424) [physics.ins-det]
- [15] Soderberg, M.: ArgoNeuT: A Liquid Argon Time Projection Chamber Test in the NuMI Beamline. In: Meeting of the Division of Particles and Fields of the American Physical Society (DPF 2009) (2009)
- [16] Cerati, G.: MicroBooNE Public Data Sets: a Collaborative Tool for LArTPC Software Development (2023). <https://arxiv.org/abs/2309.15362>
- [17] Marshall, J.S., Thomson, M.A.: The Pandora Software Development Kit for Pattern Recognition. *Eur. Phys. J. C* **75**(9), 439 (2015) <https://doi.org/10.1140/>

- [epjc/s10052-015-3659-3](https://arxiv.org/abs/1506.05348) [arXiv:1506.05348](https://arxiv.org/abs/1506.05348)
[physics.data-an]
- [18] Acciarri, R., *et al.*: The Pandora multi-algorithm approach to automated pattern recognition of cosmic-ray muon and neutrino events in the MicroBooNE detector. *Eur. Phys. J. C* **78**(1), 82 (2018) <https://doi.org/10.1140/epjc/s10052-017-5481-6> [arXiv:1708.03135](https://arxiv.org/abs/1708.03135) [hep-ex]
- [19] Abed Abud, A., *et al.*: Reconstruction of interactions in the ProtoDUNE-SP detector with Pandora. *Eur. Phys. J. C* **83**(7), 618 (2023) <https://doi.org/10.1140/epjc/s10052-023-11733-2> [arXiv:2206.14521](https://arxiv.org/abs/2206.14521) [hep-ex]
- [20] Snider, E.L., Petrillo, G.: LArSoft: Toolkit for Simulation, Reconstruction and Analysis of Liquid Argon TPC Neutrino Detectors. *J. Phys. Conf. Ser.* **898**(4), 042057 (2017) <https://doi.org/10.1088/1742-6596/898/4/042057>
- [21] Abi, B., *et al.*: Neutrino interaction classification with a convolutional neural network in the DUNE far detector. *Phys. Rev. D* **102**(9), 092003 (2020) <https://doi.org/10.1103/PhysRevD.102.092003> [arXiv:2006.15052](https://arxiv.org/abs/2006.15052) [physics.ins-det]
- [22] Machado, P., Schulz, H., Turner, J.: Tau neutrinos at DUNE: New strategies, new opportunities. *Phys. Rev. D* **102**(5), 053010 (2020) <https://doi.org/10.1103/PhysRevD.102.053010> [arXiv:2007.00015](https://arxiv.org/abs/2007.00015) [hep-ph]
- [23] Kopp, J., Machado, P., MacMahon, M., Martinez-Soler, I.: Improving Neutrino Energy Reconstruction with Machine Learning (2024) [arXiv:2405.15867](https://arxiv.org/abs/2405.15867) [hep-ph]
- [24] Moretti, R., Rossi, M., Biassoni, M., Giachero, A., Grossi, M., Guffanti, D., Labranca, D., Terranova, F., Vallecorsa, S.: Assessment of few-hits machine learning classification algorithms for low-energy physics in liquid argon detectors. *Eur. Phys. J. Plus* **139**(8), 723 (2024) <https://doi.org/10.1140/epjp/s13360-024-05287-9> [arXiv:2305.09744](https://arxiv.org/abs/2305.09744) [physics.ins-det]
- [25] Vergani, S.: A Novel Hit-Based Method to Distinguish Tracks and Showers in ProtoDUNE Single Phase. *PoS NuFact2021*, 179 (2022) <https://doi.org/10.22323/1.402.0179>
- [26] Abed Abud, A., *et al.*: Separation of track- and shower-like energy deposits in ProtoDUNE-SP using a convolutional neural network. *Eur. Phys. J. C* **82**(10), 903 (2022) <https://doi.org/10.1140/epjc/s10052-022-10791-2> [arXiv:2203.17053](https://arxiv.org/abs/2203.17053) [physics.ins-det]
- [27] Abratenko, P., *et al.*: Semantic Segmentation with Sparse Convolutional Neural Network for Event Reconstruction in MicroBooNE. *Phys. Rev. D* **103**(5), 052012 (2021) <https://doi.org/10.1103/PhysRevD.103.052012> [arXiv:2012.08513](https://arxiv.org/abs/2012.08513) [physics.ins-det]
- [28] Bermejo, P., Braccia, P., Rudolph, M.S., Holmes, Z., Cincio, L., Cerezo, M.: Quantum Convolutional Neural Networks are (Effectively) Classically Simulable (2024) [arXiv:2408.12739](https://arxiv.org/abs/2408.12739) [quant-ph]
- [29] Bowles, J., Ahmed, S., Schuld, M.: Better than classical? The subtle art of benchmarking quantum machine learning models (2024) [arXiv:2403.07059](https://arxiv.org/abs/2403.07059) [quant-ph]
- [30] Chen, S.Y.-C., Wei, T.-C., Zhang, C., Yu, H., Yoo, S.: Hybrid quantum-classical graph convolutional network. *arXiv preprint arXiv:2101.06189* (2021)
- [31] Chen, S.Y.-C., Wei, T.-C., Zhang, C., Yu, H., Yoo, S.: Quantum convolutional neural networks for high energy physics data analysis. *Physical Review Research* **4**(1), 013231 (2022)
- [32] Delgado, A., Venegas-Vargas, D., Huynh, A., Carroll, K.: Towards designing scalable quantum-enhanced generative networks for neutrino physics experiments with liquid argon time projection chambers. *arXiv preprint arXiv:2410.12650* (2024)
- [33] Di Meglio, A., Doser, M., Frisch, B., Grabowska, D.M., Pierini, M., Vallecorsa, S.:

- CERN Quantum Technology Initiative Strategy and Roadmap (2021) <https://doi.org/10.5281/zenodo.5571809>
- [34] Bharti, K., Cervera-Lierta, A., Kyaw, T.H., Haug, T., Alperin-Lea, S., Anand, A., Degroote, M., Heimonen, H., Kottmann, J.S., Menke, T., Mok, W.-K., Sim, S., Kwek, L.-C., Aspuru-Guzik, A.: Noisy intermediate-scale quantum algorithms. *Reviews of Modern Physics* **94**(1) (2022) <https://doi.org/10.1103/revmodphys.94.015004>
- [35] Zheng, H., Li, Z., Liu, J., Strelchuk, S., Kondor, R.: Speeding up learning quantum states through group equivariant convolutional quantum ansätze. *PRX Quantum* **4**(2) (2023) <https://doi.org/10.1103/prxquantum.4.020327>
- [36] Du, Y., Hsieh, M.-H., Liu, T., Tao, D.: Expressive power of parametrized quantum circuits. *Physical Review Research* **2**(3) (2020) <https://doi.org/10.1103/physrevresearch.2.033125>
- [37] Coyle, B., Mills, D., Danos, V., Kashefi, E.: The born supremacy: quantum advantage and training of an ising born machine. *npj Quantum Information* **6**(1) (2020) <https://doi.org/10.1038/s41534-020-00288-9>
- [38] Jäger, J., Krams, R.V.: Universal expressiveness of variational quantum classifiers and quantum kernels for support vector machines. *Nature Communications* **14**(1) (2023) <https://doi.org/10.1038/s41467-023-36144-5>
- [39] Sweke, R., Recio, E., Jerbi, S., Gil-Fuster, E., Fuller, B., Eisert, J., Meyer, J.J.: Potential and limitations of random Fourier features for dequantizing quantum machine learning (2025). <https://arxiv.org/abs/2309.11647>
- [40] Huang, H.-Y., Broughton, M., Mohseni, M., Babbush, R., Boixo, S., Neven, H., McClean, J.R.: Power of data in quantum machine learning. *Nature Communications* **12**(1) (2021) <https://doi.org/10.1038/s41467-021-22539-9>
- [41] Cerezo, M., Larocca, M., García-Martín, D., Diaz, N.L., Braccia, P., Fontana, E., Rudolph, M.S., Bermejo, P., Ijaz, A., Thanasilp, S., et al.: Does provable absence of barren plateaus imply classical simulability? or, why we need to rethink variational quantum computing. arXiv preprint arXiv:2312.09121 (2023)
- [42] Duffy, C., Hassanshah, M., Jastrzebski, M., Malik, S.: Unsupervised Beyond-Standard-Model Event Discovery at the LHC with a Novel Quantum Autoencoder (2024). <https://arxiv.org/abs/2407.07961>
- [43] Duckett, P., Facini, G., Jastrzebski, M., Malik, S., Scanlon, T., Rettie, S.: Reconstructing charged particle track segments with a quantum-enhanced support vector machine. *Phys. Rev. D* **109**, 052002 (2024) <https://doi.org/10.1103/PhysRevD.109.052002>
- [44] Tüysüz, C., Demidik, M., Coopmans, L., Rinaldi, E., Croft, V., Haddad, Y., Rosenkranz, M., Jansen, K.: Learning to generate high-dimensional distributions with low-dimensional quantum boltzmann machines. arXiv preprint arXiv:2410.16363 (2024)
- [45] Ragone, M., Braccia, P., Nguyen, Q.T., Schatzki, L., Coles, P.J., Sauvage, F., Larocca, M., Cerezo, M.: Representation Theory for Geometric Quantum Machine Learning (2023). <https://arxiv.org/abs/2210.07980>
- [46] Nguyen, Q.T., Schatzki, L., Braccia, P., Ragone, M., Coles, P.J., Sauvage, F., Larocca, M., Cerezo, M.: Theory for equivariant quantum neural networks. *PRX Quantum* **5**(2) (2024) <https://doi.org/10.1103/prxquantum.5.020328>
- [47] Meyer, J.J., Mularski, M., Gil-Fuster, E., Mele, A.A., Arzani, F., Wilms, A., Eisert, J.: Exploiting symmetry in variational quantum machine learning. *PRX Quantum* **4**(1) (2023) <https://doi.org/10.1103/prxquantum.4.010328>
- [48] Paine, A.E., Elfving, V.E., Kyriienko, O.:

- Physics-Informed Quantum Machine Learning: Solving nonlinear differential equations in latent spaces without costly grid evaluations (2023). <https://arxiv.org/abs/2308.01827>
- [49] Kyriienko, O., Paine, A.E., Elfving, V.E.: Protocols for trainable and differentiable quantum generative modeling. *Physical Review Research* **6**(3) (2024) <https://doi.org/10.1103/physrevresearch.6.033291>
- [50] Williams, C.A., Scali, S., Gentile, A.A., Berger, D., Kyriienko, O.: Addressing the Readout Problem in Quantum Differential Equation Algorithms with Quantum Scientific Machine Learning (2024). <https://arxiv.org/abs/2411.14259>
- [51] Cong, I., Choi, S., Lukin, M.D.: Quantum convolutional neural networks. *Nature Physics* **15**(12), 1273–1278 (2019)
- [52] Abratenko, P., et al.: MicroBooNE BNB Inclusive Overlay Sample (No Wire Info). <https://doi.org/10.5281/zenodo.8370883>
- [53] Abratenko, P., et al.: Vertex-finding and reconstruction of contained two-track neutrino events in the microboone detector. *Journal of Instrumentation* **16**(02), 02017–02017 (2021) <https://doi.org/10.1088/1748-0221/16/02/p02017>
- [54] Chappell, A., Whitehead, L.H.: Application of transfer learning to neutrino interaction classification. *Eur. Phys. J. C* **82**(12), 1099 (2022) <https://doi.org/10.1140/epjc/s10052-022-11066-6> [arXiv:2207.03139](https://arxiv.org/abs/2207.03139) [hep-ex]
- [55] Agostinelli, S., et al.: GEANT4: A Simulation toolkit. *Nucl. Instrum. Meth. A* **506**, 250–303 (2003) [https://doi.org/10.1016/S0168-9002\(03\)01368-8](https://doi.org/10.1016/S0168-9002(03)01368-8)
- [56] Abi, B., et al.: Deep Underground Neutrino Experiment (DUNE), Far Detector Technical Design Report, Volume IV: Far Detector Single-phase Technology. *JINST* **15**(08), 08010 (2020) <https://doi.org/10.1088/1748-0221/15/08/T08010> [arXiv:2002.03010](https://arxiv.org/abs/2002.03010) [physics.ins-det]
- [57] Krizhevsky, A., Sutskever, I., Hinton, G.E.: Imagenet classification with deep convolutional neural networks. In: Pereira, F., Burges, C.J., Bottou, L., Weinberger, K.Q. (eds.) *Advances in Neural Information Processing Systems*. Curran Associates, Inc.
- [58] He, K., Zhang, X., Ren, S., Sun, J.: Deep Residual Learning for Image Recognition (2015). <https://arxiv.org/abs/1512.03385>
- [59] Ronneberger, O., Fischer, P., Brox, T.: U-net: Convolutional networks for biomedical image segmentation. In: Navab, N., Hornegger, J., Wells, W.M., Frangi, A.F. (eds.) *Medical Image Computing and Computer-Assisted Intervention – MICCAI 2015*, pp. 234–241. Springer, Cham (2015)
- [60] Rombach, R., Blattmann, A., Lorenz, D., Esser, P., Ommer, B.: High-resolution image synthesis with latent diffusion models. 2022 IEEE/CVF Conference on Computer Vision and Pattern Recognition (CVPR), 10674–10685 (2021)
- [61] Domin, L., Terao, K.: Scalable deep convolutional neural networks for sparse, locally dense liquid argon time projection chamber data. *Physical Review D* **102**(1) (2020) <https://doi.org/10.1103/physrevd.102.012005>
- [62] Liu, J., Ott, J., Collado, J., Jargowsky, B., Wu, W., Bian, J., Baldi, P.: Deep-Learning-Based Kinematic Reconstruction for DUNE (2020) [arXiv:2012.06181](https://arxiv.org/abs/2012.06181) [physics.ins-det]
- [63] Adhikari, M., Adhikari, A.: *Basic Modern Algebra with Applications*. Springer, New Delhi (2014). <https://doi.org/10.1007/978-81-322-1599-8>
- [64] Worrall, D., Brostow, G.: Cubenet: Equivariance to 3d rotation and translation. In: *Proceedings of the European Conference on Computer Vision (ECCV)*, pp. 567–584 (2018)

- [65] Cohen, T.S., Geiger, M., Weiler, M.: A general theory of equivariant cnns on homogeneous spaces. *Advances in neural information processing systems* **32** (2019)
- [66] Weiler, M., Cesa, G.: General e (2)-equivariant steerable cnns. *Advances in neural information processing systems* **32** (2019)
- [67] Henderson, M.P., Shakya, S., Pradhan, S., Cook, T.: Quanvolutional neural networks: powering image recognition with quantum circuits. *Quantum Machine Intelligence* **2** (2019)
- [68] Liu, J., Lim, K.H., Wood, K.L., Huang, W., Guo, C., Huang, H.-L.: Hybrid quantum-classical convolutional neural networks. *Science China Physics, Mechanics & Astronomy* **64**(9) (2021) <https://doi.org/10.1007/s11433-021-1734-3>
- [69] Quanvolutional Neural Networks. <https://pennylane.ai/qml/demos/tutorial-quanvolution#quanvolutional-neural-networks>. Accessed: 07-02-2025
- [70] Ding, X., Zhang, X., Han, J., Ding, G.: Scaling up your kernels to 31x31: Revisiting large kernel design in cnns. In: *Proceedings of the IEEE/CVF Conference on Computer Vision and Pattern Recognition*, pp. 11963–11975 (2022)
- [71] Liu, S., Chen, T., Chen, X., Chen, X., Xiao, Q., Wu, B., Kärkkäinen, T., Pechenizkiy, M., Mocanu, D., Wang, Z.: More convnets in the 2020s: Scaling up kernels beyond 51x51 using sparsity. *arXiv preprint arXiv:2207.03620* (2022)
- [72] Schatzki, L., Larocca, M., Nguyen, Q.T., Sauvage, F., Cerezo, M.: Theoretical guarantees for permutation-equivariant quantum neural networks. *npj Quantum Information* **10**(1) (2024) <https://doi.org/10.1038/s41534-024-00804-1>
- [73] Gonzalez, R.C., Woods, R.E.: *Digital Image Processing*, 3rd edn. Pearson, ??? (2007)
- [74] Dummit, D.S., Foote, R.M.: *Abstract Algebra*, 3rd edn. John Wiley & Sons, ??? (2003)
- [75] Moritz, P., Nishihara, R., Wang, S., Tumanov, A., Liaw, R., Liang, E., Elibol, M., Yang, Z., Paul, W., Jordan, M.I., *et al.*: Ray: A distributed framework for emerging {AI} applications. In: *13th USENIX Symposium on Operating Systems Design and Implementation (OSDI 18)*, pp. 561–577 (2018)
- [76] Biewald, L.: Experiment Tracking with Weights and Biases. Software available from wandb.com (2020). <https://www.wandb.com/>
- [77] Sein, P.S.S., Cañizo, M., Orús, R.: Image classification with rotation-invariant variational quantum circuits. *Physical Review Research* **7**(1) (2025) <https://doi.org/10.1103/physrevresearch.7.013082>